Electronic Supplementary Information

for

Plasma-assisted fabrication of ultra-dispersed copper oxides

in and *on* C-rich carbon nitride

as functional composites for the oxygen evolution reaction

Mattia Benedet,[a,b] Angelica Fasan,[b] Davide Barreca,[b] Chiara Maccato,*[a,b]

Cinzia Sada,[c] Silvia Maria Deambrosis,[b] Valentina Zin,[b] Francesco Montagner,[b]

Oleg I. Lebedev,[d] Evgeny Modin,[e] Gian Andrea Rizzi[a,b] and Alberto Gasparotto[a,b]

[a.] *Department of Chemical Sciences -Padova University and INSTM, 35131 Padova, Italy.*

[b.] *CNR-ICMATE and INSTM, 35127 Padova, Italy.*

[c.] *Department of Physics and Astronomy, Padova University and INSTM, 35131 Padova, Italy.*

[d.] *Laboratoire CRISMAT, UMR 6508 Normandie Université, CNRS, ENSICAEN, UNICAEN, 14050 Caen Cedex 4, France.*

[e.] *CIC nanoGUNE BRTA, 20018 Donostia, San Sebastian, Spain.*

* Author to whom correspondence should be addressed; e-mail: chiara.maccato@unipd.it.

Table of Contents

§ S1. Experimental

§ S1.1 Synthesis

Prior to deposition of a-CN$_x$, the Ar pressure in the reaction chamber was set to 7.0×10^{-7} mbar and the power was gradually raised from 20 W to 100 W (rate = 20 W/min), to clean the pyrolytic graphite target mounted on the radio-frequency (RF) electrode and reduce the formation of cracks generally resulting from thermal or mechanical shocks.

§ S1.2 Characterization

X-ray diffraction (XRD) measurements were performed by a Bruker AXS D8 Advance Plus diffractometer equipped with a Göbel mirror and a CuKα X-ray source (λ = 1.54051 Å) powered at 40 kV, 40 mA. The latter were carried out at the PanLab facility (Department of Chemical Sciences, Padova University) founded by the MIUR Dipartimento di Eccellenza grant "NExuS".

UV-Vis optical spectra were collected on a FLS1000 fluorimeter (Edinburgh Instruments) equipped with a Xe arc lamp, a single/double grating Czerny-Turner monochromator and a cool-housed (22°C) PMT-900 detector. Analyses were performed in diffuse reflectance mode in the 300-800 nm range (spectral bandwidth = 1 nm). Absorption edge evaluation was performed using the Tauc equation [f(R)hv]^n *vs*. hv, where f(R) is the Kubelka-Munk function and R is the reflectance, assuming n = ½.[1-4]

X-ray photoelectron spectroscopy (XPS), ultraviolet photoelectron spectroscopy (UPS), ion scattering spectroscopy (ISS) and reflection electron energy loss spectroscopy (REELS) measurements were performed with an ESCALAB™ QXi Spectrometer funded by "Sviluppo delle infrastrutture e programma biennale degli interventi del Consiglio Nazionale delle Ricerche (2019)". In UPS valence band spectra, the cut-off position was found by fitting the linear part of the low kinetic energy side of the spectrum and calculating the intercept with the X-axis. REELS spectra acquired using a primary electron beam energy of 1000 eV.

Root-mean-square (RMS) roughness values were obtained from 3×3 μm^2 atomic force microscopy (AFM) images, as previously reported.[2] The uncertainty on the reported values is ± 0.2 nm.

Cross-sectional samples for transmission electron microscopy (TEM) analyses were prepared by means of the focused ion beam (FIB) technique using a Tescan Amber X apparatus. Pre-thinned lamellas were lifted out from the target material, attached to TEM grids and thinned down to electron transparency. Final cleaning was performed by FIB at 5 kV and 25 pA. During preparation, a Pt protective layer was deposited on the samples in order to prevent the occurrence of undesired

alterations.

Hardness (H) and elastic modulus (E) were measured by instrumented nanoindentation (NanoTest, Micro Materials, Wrexham, UK) equipped with a sharp Berkovich diamond probe [elastic modulus (E) = 1140 GPa and Poisson ratio (v) = 0.07]. Tests were performed in depth control, with a maximum penetration depth of 40 nm, so that the ratio between penetration depth (d) and coating thickness (h) was d/h < 0.1, to minimize the FTO substrate influence.[5] A statistical analysis was carried out on 25 indentations for each specimen, distributed into 5×5 grids. The resulting load-displacement curves were elaborated using the Oliver and Pharr method, to estimate the hardness and the elastic modulus of the analysed surfaces[6, 7].

Film-to-substrate adhesion was investigated *via* scratch tests, conducted using a UMT-2 tribotester (Bruker), equipped with a standard Rockwell C diamond tip. Test parameters were selected from EN ISO 20502:2016 standard for ceramic materials by scratch testing.[8] In a scratch test, an increasing force normal to the surface under test is applied to the stylus, to promote adhesive and/or cohesive failure of the coating-substrate system. Typical consecutive coating failure events occur, named critical loads, Lc [N]. The onset of cracking is then characterized by the critical normal load Lc1, while the onset of coating spallation is defined as critical normal load Lc3. Overall, the investigation of mechanical properties of CN_x-based films is relevant not only for an eventual application of such materials as protective coatings but also, in the case of photoelectrochemical applications, to assess the mechanical/operational stability of the developed electrodes and related film/substrate adhesion.

From linear sweep voltammetry (LSV) curves, the onset potential was calculated as the one necessary to reach a current density of 0.02 mA/cm^2.[1, 9, 10]

The obtained potential values [V *vs.* the reversible hydrogen electrode (RHE), E_{RHE}] were subjected to *iR* correction according to equation:[10]

$$E \ (V) = E_{RHE} \ (V) - iR \tag{S1}$$

where *i* is the measured current (in A), and *R* the uncompensated cell resistance. The latter was estimated by impedance spectroscopy (EIS) measurements in the high-frequency region of Nyquist plots.

Applied bias photon-to-current efficiency (ABPE) curves were obtained through the equation:[10, 11]

ABPE (%) = ([j_{photo} × (1.23 − E)]/P) × 100 (S2)

where j_{photo} (μA/cm^2) is the photocurrent density at the potential E [V *vs.* the reversible hydrogen electrode (RHE)] and P is the incident light intensity (50 mW/cm^2, emitted from a white LED source spanning continuously between 400 and 800 nm with two maxima located at ≈ 440 nm and ≈ 560 nm), measured by a feedback loop. Chronoamperometry (CA) analyses were carried out at a fixed potential of 1.65 V *vs.* RHE.

# § S2. Additional chemico-physical characterization results
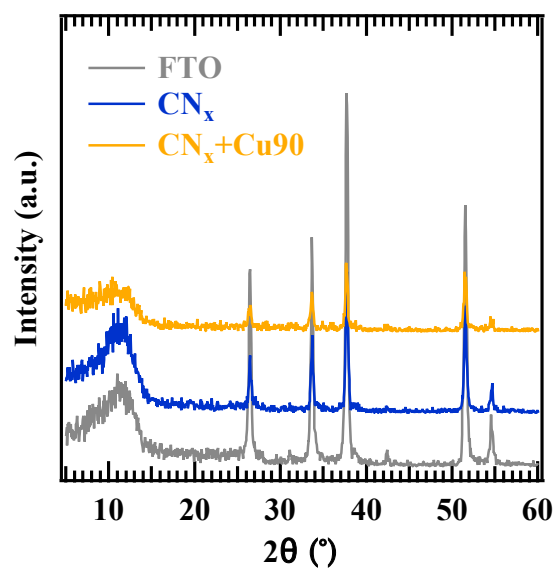
Fig. S1. XRD patterns for representative samples, recorded in glancing incidence mode (θ_i = 2.0°). As shown by the comparison with the pattern of the FTO substrate, only the signals related to the latter were observed.
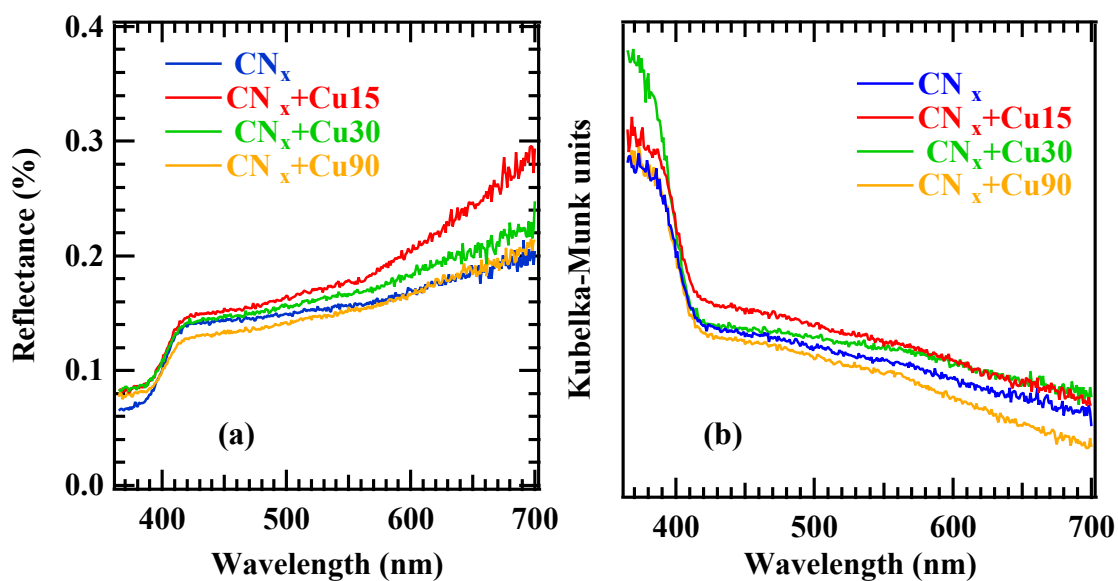
Fig. S2. Optical spectra collected in reflectance (a) and in Kubelka-Munk units (b) for the target samples.

The recorded optical spectra were characterized by a progressive increase in light absorption from 700 nm to ≈400 nm. The intense absorption for wavelengths lower than 400 nm, corresponding to the interband transitions of carbon nitride materials, was more pronounced for samples CN_x+Cu15 and CN_x+Cu30, the best performing ones (see electrochemical tests).

X-ray photoelectron spectroscopy (XPS) measurements were performed on the fabricated materials and, for comparison, on a specimen prepared by sputtering copper for 90 min directly on FTO (labelled as FTO+Cu90). For bare carbon nitride, the survey spectrum (Fig. S3) was characterized by C, N, and O photoelectron and Auger peaks, whereas no signals attributable to FTO were detected, indicating a complete substrate coverage. For composite specimens, beside the above signals, even copper ones were detected. These findings demonstrate the successful functionalization of carbon nitride with relatively low copper amounts (see Table S1), yielding a heterocomposite surface where CN_x was only partially covered by Cu-containing aggregates.

For the FTO+Cu90 sample, even tin signals from the underlying FTO substrate were observed.
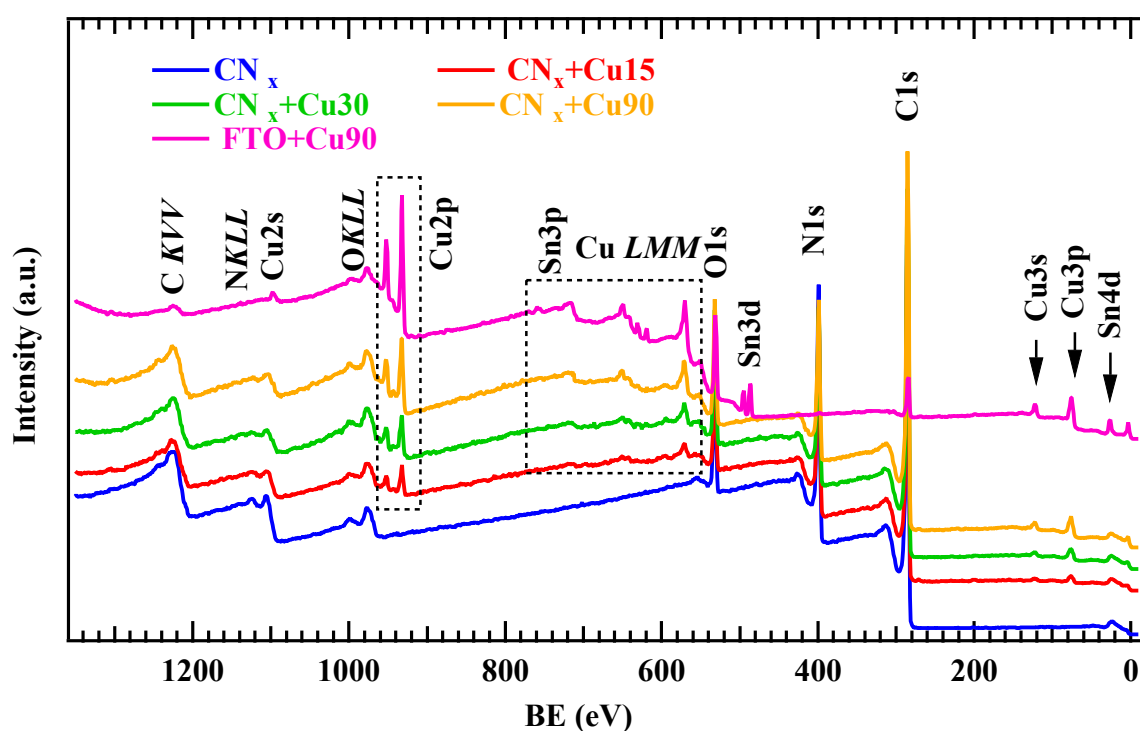
Fig. S3. Wide scan XP spectra for bare and functionalized CN_x-based samples. The spectrum of specimen FTO+Cu90 is also displayed for comparison.

| Sample	CN_x	CN_x+Cu15	CN_x+Cu30	CN_x+Cu90
C at.%	66.9	66.4	68.2	68.7
N at.%	26.7	25.5	20.9	19.7
O at.%	6.4	7.3	9.8	9.7
Cu at.%	0.0	0.8	1.1	1.9
N/C	0.40	0.38	0.31	0.29
Cu/N	0.00	0.032	0.052	0.095

Table S1. XPS atomic percentages (at.%) and corresponding N/C and Cu/N ratios for bare CN_x and Cu_xO-functionalized samples.

Quantitative analyses enabled the following general conclusions:

i) for all specimens, carbon was the predominant element [average value ≈ (67.5±1.2) at.%], with a content ≈2.5-3.5 times higher than nitrogen. Although the overall C amount was also affected by adventitious species arising from air exposure, the obtained results (see also the main paper text) are consistent with the occurrence of carbon-rich (partially graphitic) CN_x materials incorporating up to ≈27% of nitrogen, in line with previous studies.[12-14] Interestingly, the N/C ratio progressively decreased from ≈0.4 to ≈0.3 upon going from sample CN_x to CN_x+Cu90, *i.e.* for longer Cu deposition times. Taking into account also SIMS results (see Fig. 4 and pertaining discussion) this phenomenon, consistent with the trend of the various C1s peak components in Fig. 3c, can be explained considering that the plasma-assisted deposition of Cu-containing species induces the sputtering of both carbon and nitrogen from the underlying CN_x matrix, with nitrogen being preferentially removed with respect to carbon.

ii) all samples contained non-negligible amounts of oxygen, likely originating from the desorption of residual water from the walls of the reaction chamber, the exposure of the carbon nitride matrix to air and, for composite systems, also from the oxidation of copper nanoparticles. As discussed in the main paper text, the presence of oxygen species on CN_x was found to promote an enhanced oxidation of copper, leading to the formation of Cu(I)/Cu(II) species. In this regard, the occurrence

of CN_x-O-Cu bonding interactions, besides "anchoring" copper particles to the underlying deposit, is expected to favour charge transfer events at the interface between the two materials.[15, 16]
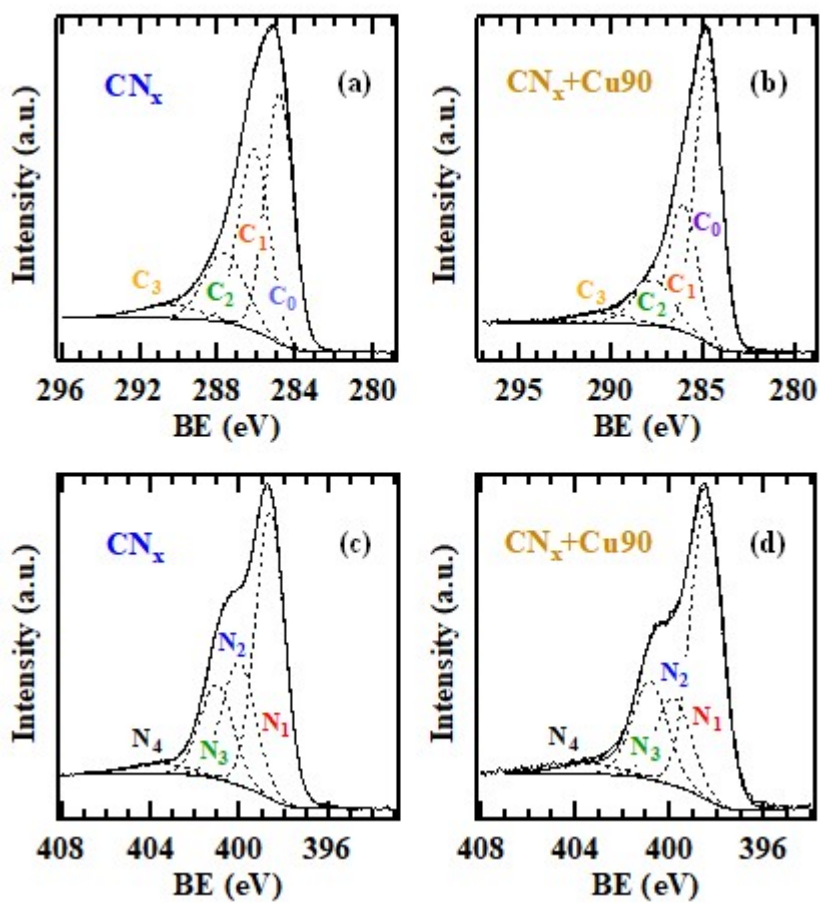
Fig. S4. Deconvolution of (a,b) C1s and (c,d) N1s peaks for specimens CN_x and CN_x+Cu90.
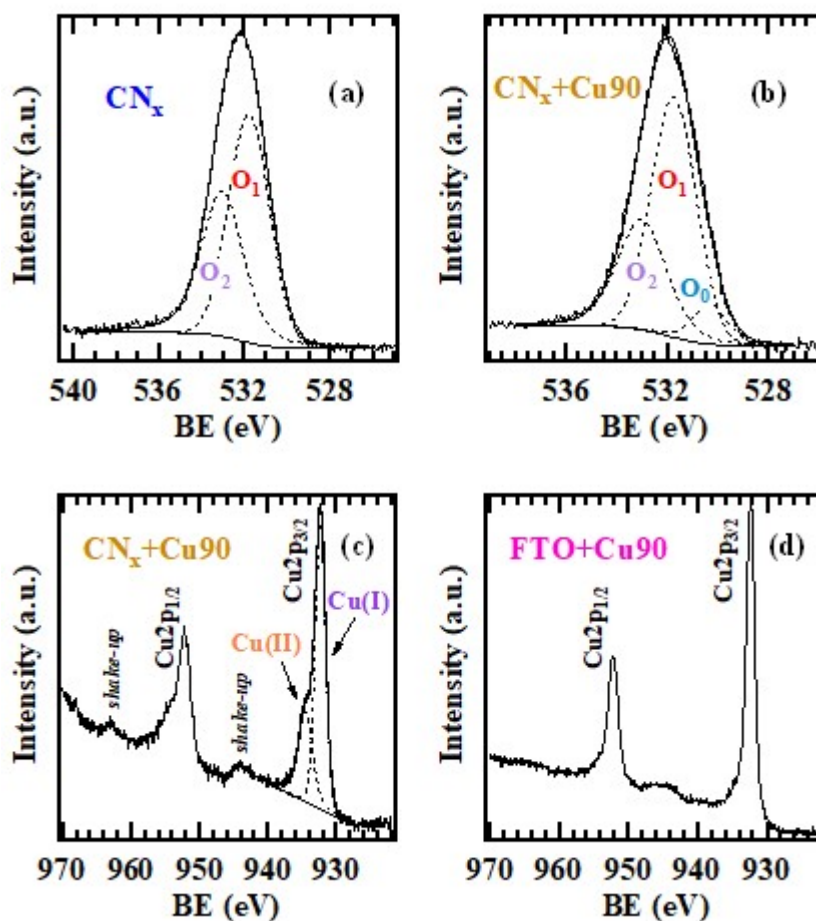
Fig. S5. O1s signal for specimens (a) CN_x and (b) CN_x+Cu90. The contribution of the O_0 lattice oxygen component to the overall peak area increased with copper sputtering time (from ≈3% for CN_x+Cu15, to ≈9% for CN_x+Cu90). Cu2p signal for (c) CN_x+Cu90 and (d) FTO+Cu90.
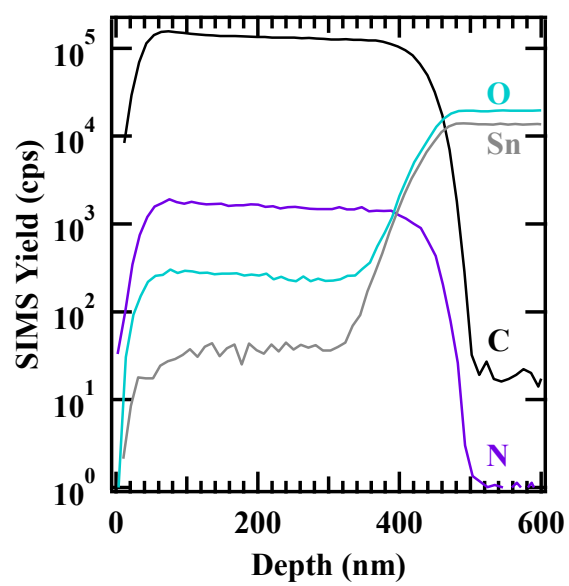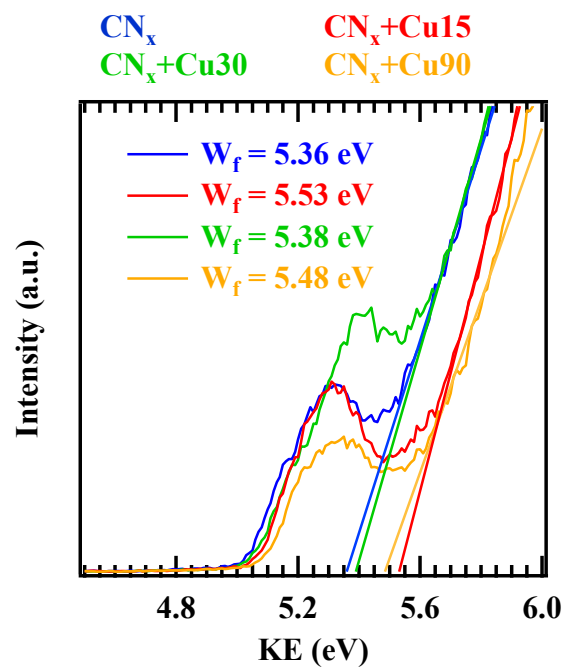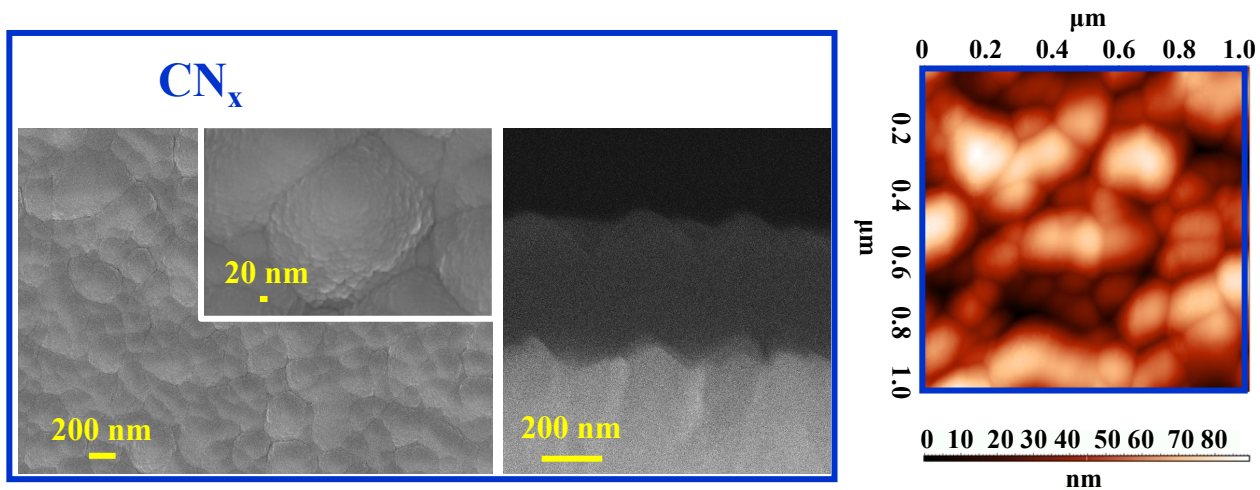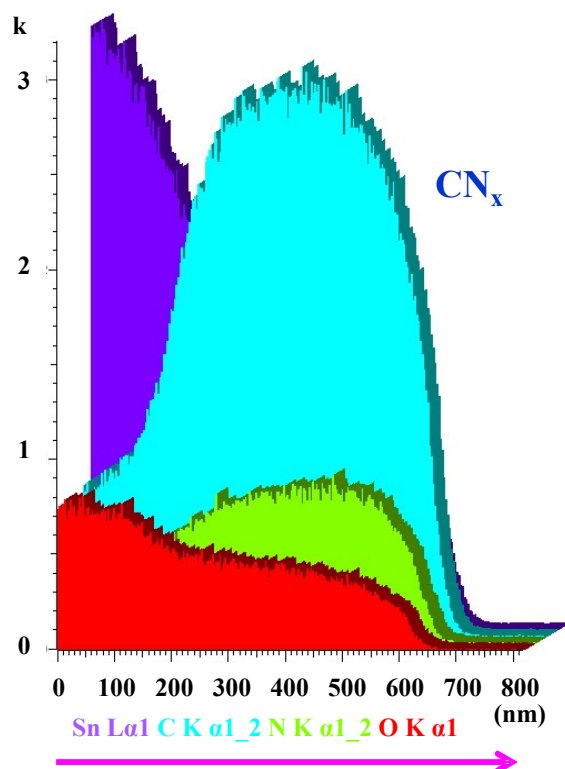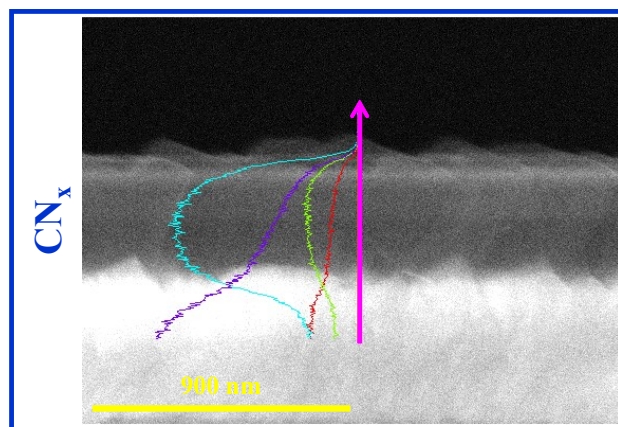
**Fig. S6**. SIMS depth profile for bare CN_x.

Fig. S7. Enlargement of Fig. 5a, evidencing the intercept obtained by fitting the linear part of UPS valence band spectra for the evaluation of work function.

Fig. S8. Plane-view and cross-sectional FE-SEM images (left and central panel, respectively), and AFM micrographs (right panel) for bare CN_x.
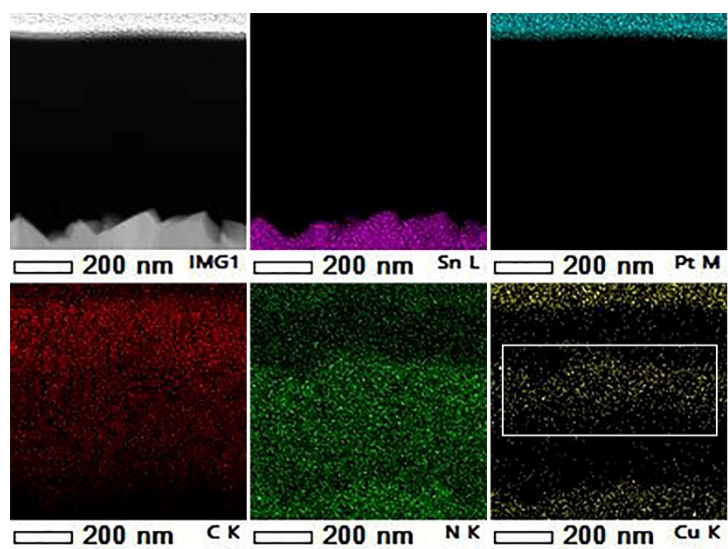
Fig. S9. Cross-sectional EDXS line scans for bare CN$_x$, recorded along the arrow marked in the reported FE-SEM micrograph.
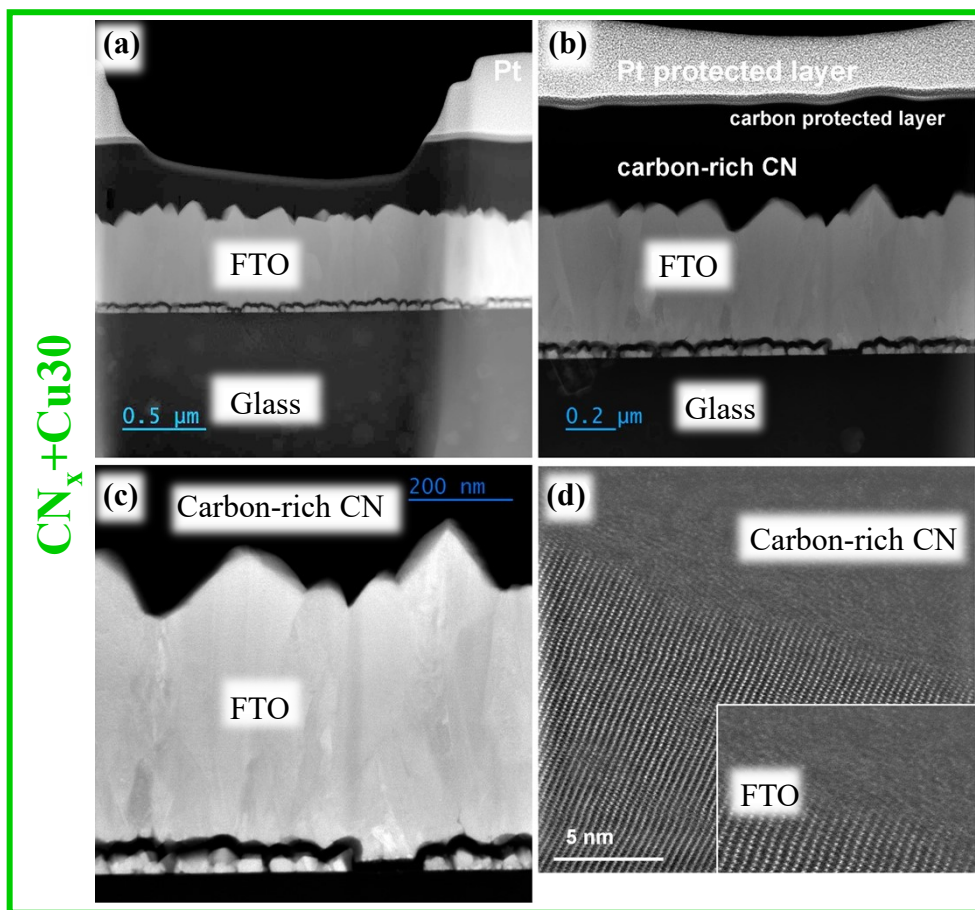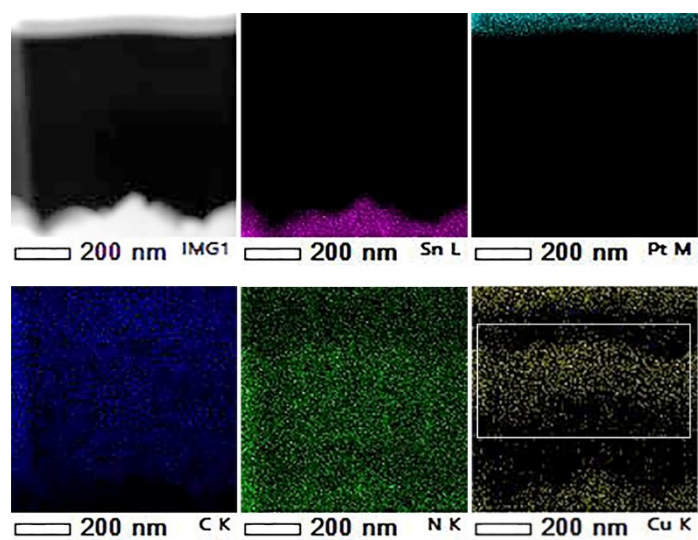
Fig. S10. (a-c) Low resolution cross-sectional HAADF-STEM images of sample CN_x+Cu30 at different magnifications; (d) high resolution HAADF-STEM image of FTO/a-CN_x interface. The inset displays a magnified area.
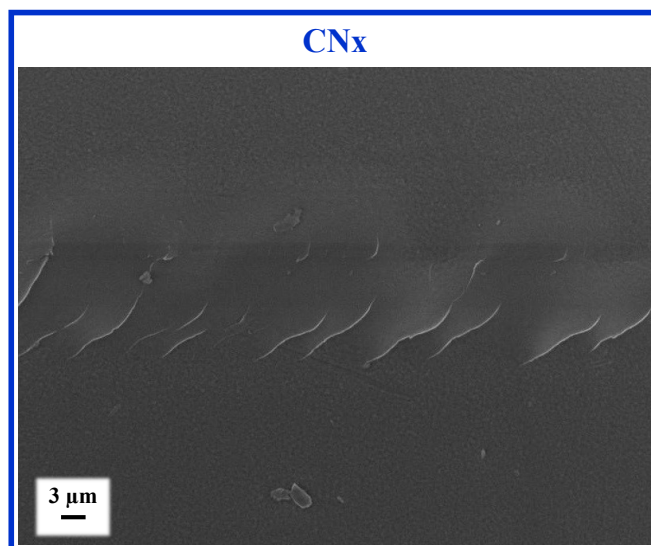
Fig. S11. EDXS-STEM elemental maps of Sn L, Pt M, C K, N K, and Cu K for specimen CN_x+Cu15.

Fig. S12. EDXS-STEM elemental maps of Sn L, Pt M, C K, N K, and Cu K for specimen CN$_x$+Cu30.

Fig. S13. SEM image for sample CN_x after the scratch test. The blistering effect occurring between the film and the substrate, resulting in the formation of cracks due to an adhesive-like breakage, is clearly evident. The lack of plastic deformation and the brittle fracture are a consequence of the amorphous structure.
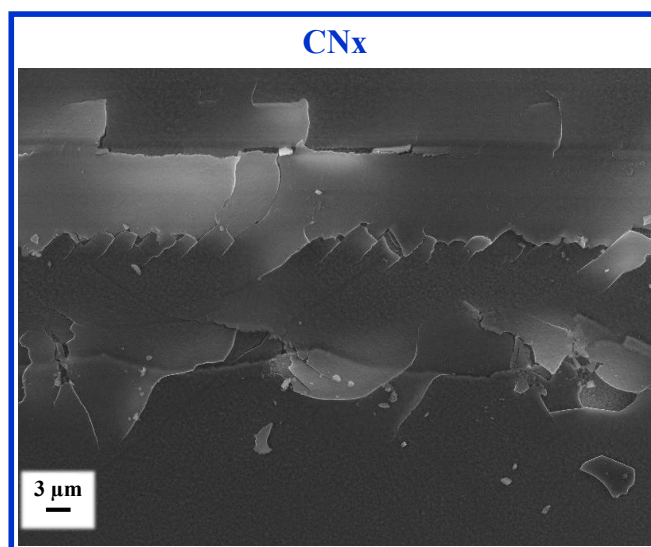
Fig. S14. SEM image for sample CN_x, showing the film chipping and spallation after the blistering phenomenon as the applied normal load exceeds the critical value for the deposit detachment from the substrate.

A similar failure mechanism is observed in all the tested samples. Initially, the passage of the diamond tip triggers shear stresses, compressing the film in front, and causing swelling at the deposit/FTO interface (Fig. S13). This effect, called "blistering", is progressively intensified, until the formation of the first cracks followed by catastrophic film chipping and spallation (Fig. S14). The

spallation is characterized by the coating detachment, to minimize the amount of elastic energy stored by the large compressive stresses ahead of the moving stylus.[17] This failure mode, typical of brittle materials, generally leaves signs of damage in the track as well as chipping along its edges, indicating weak cohesive strength of the deposit material. When the cracks are generated and the first weak acoustic emissions are recorded, after the load exceeds the critical value Lc, film failure occurs. The breakage profiles of the films are very sharp and serrated, without signs of plastic deformation. The results indicate the brittle behavior of the deposit, in line with the amorphous character of carbon nitride, that is uncapable of undergoing plastic deformations before breaking.
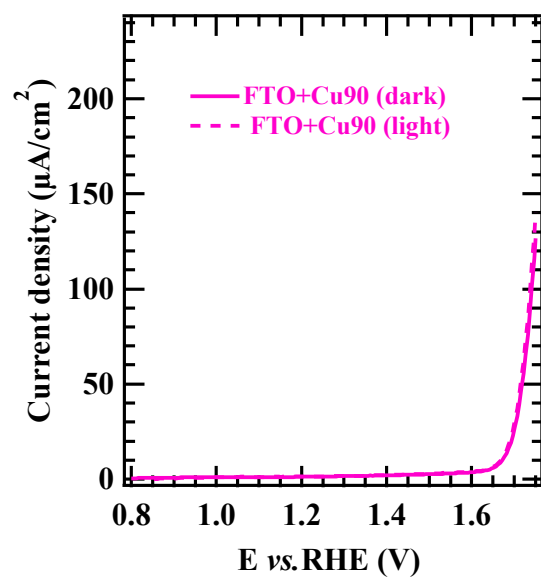
Fig. S15. LSV curves collected in the dark (continuous line) and under illumination (dotted line) for a reference sample prepared by copper sputtering for 90 min on the bare FTO substrate.
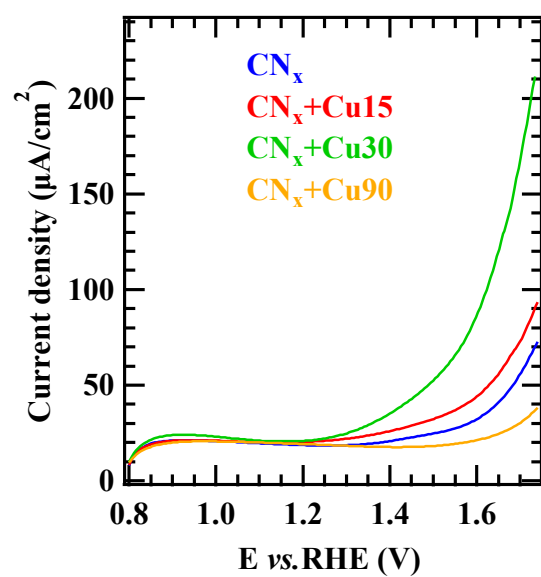
Fig. S16. LSV curves collected in the dark for the target specimens.
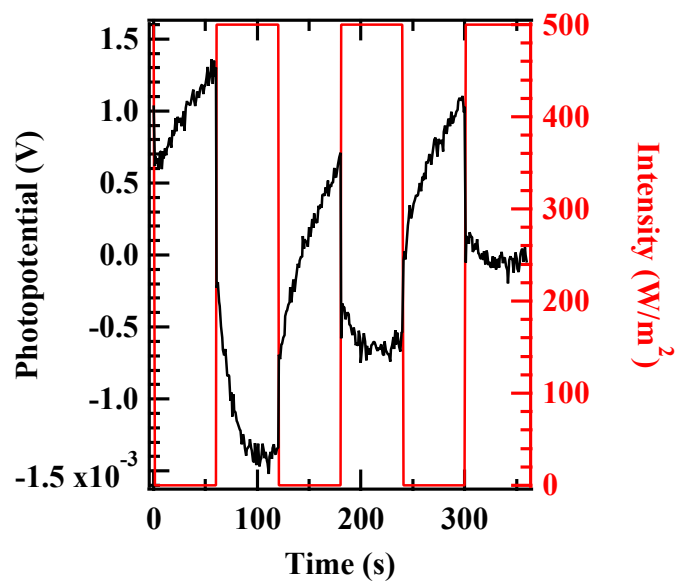
Fig. S17. Photopotential scan (left axis) as a function of time measured at the open circuit potential (OCP) with intermittent light intensity (right axis) for a representative CN$_x$+Cu sample.
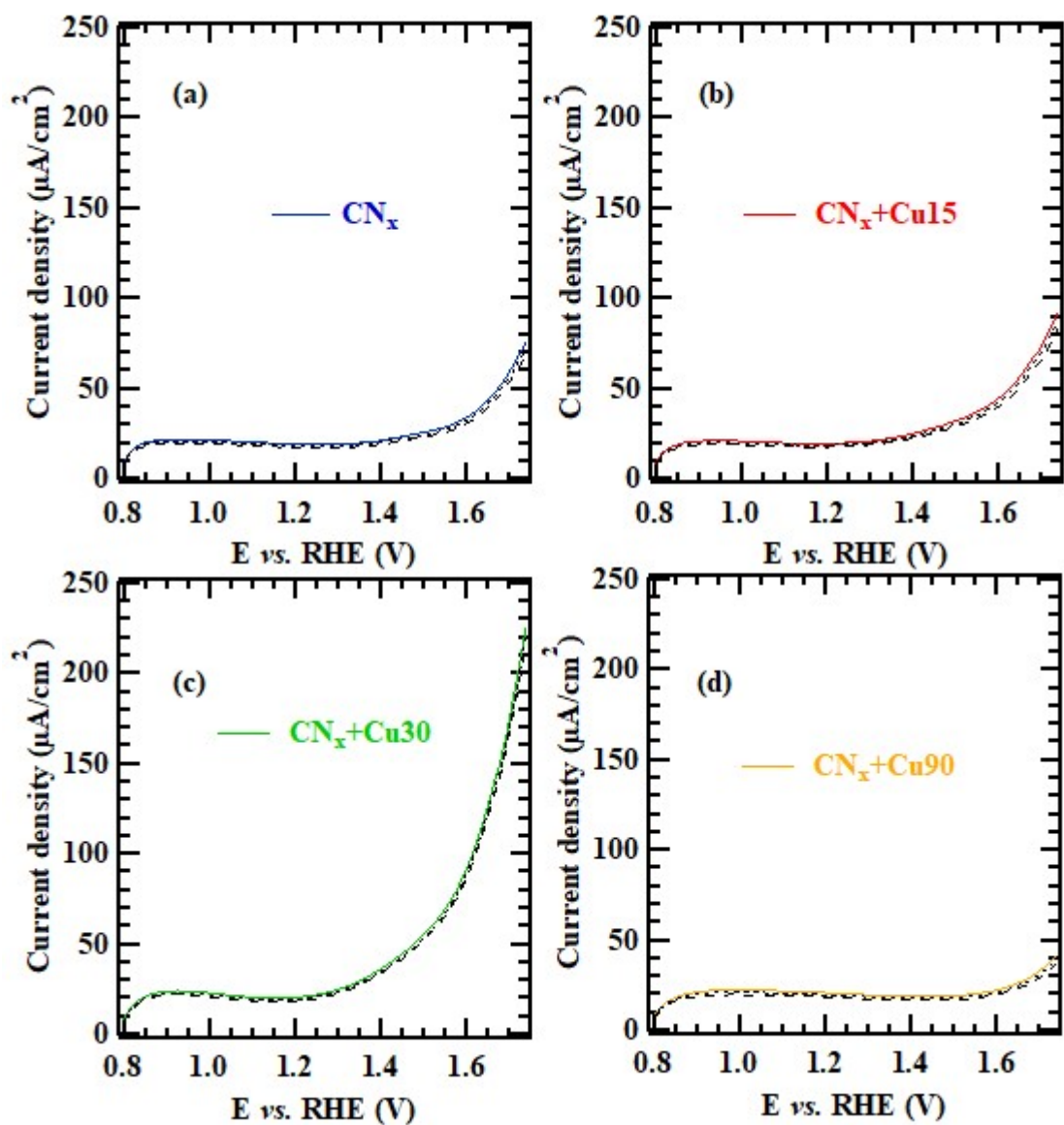
Fig. S18. j-V curves collected on as-prepared samples (continuous line) and repeated after 90 and 180 days (dashed and dotted lines, respectively) for the labelled specimens, upon sample storage under ambient conditions.

| Material	Electrolyte	$j_{1.65}$ $(\mu A/cm^2)$	E_{onset} (mV_{RHE})	$ABPE_{max}$ $(\times 10^{-3})$	E_{Wmax} (mV_{RHE})
CN$_x$		42.4	880	6.2	870
CN$_x$+Cu15	KOH 0.1 M	55.6	850	7.6	870
CN$_x$+Cu30		125.8	840	8.3	850
CN$_x$+Cu90		25.5	880	5.4	860

Table S2. Oxygen evolution reaction (OER) performances for photoelectrocatalysts based on CN$_x$ and Cu$_x$O, in alkaline water splitting. $j_{1.65}$ corresponds to the current density measured at 1.65 V *vs.* RHE. The potential of maximum efficiency (E_{Wmax}) corresponds to the maximum in each of the ABPE curves plotted in Fig. 10c.

Sample	Electrolyte	$j_{1.65}$ (μA/cm^2)	Ref.
gCN [a]	HClO$_4$ (pH = 3)	< 0.1 [b]	[18]
gCN	Na$_2$SO$_4$ 0.2 M	15 [c]	[19]
gCN	Na$_2$SO$_4$ 0.2 M	0 [b]	[20]
gCN	KOH 1.0 M	$\approx$ 9.0 [c]	[2]
gCN	KOH 1.0 M	0 [c]	[21]
gCN	KOH 1.0 M	$\approx$ 50 [b]	[22]
gCN	NaOH 0.1 M	$\approx$ 20 [c]	[23]
gCN	Na$_2$SO$_4$ 0.3 M	$\approx$ 24 [c,d]	[24]
Co$_3$O$_4$/gCN	Na$_2$SO$_4$ 0.2 M	0 [b]	[20]
NiO-CN$_x$ [e]	Na$_2$SO$_4$ 0.5 M (pH = 6)	$\approx$ 0.3 [c]	[25]
Ni(OH)$_2$/gCN	NaOH 0.1 M	$\approx$ 30 $\div$ $\approx$ 40 [c]	[23]
ZnO/gCN	Na$_2$SO$_4$ 0.3 M	$\approx$ 172 [c,d]	[24]
CoFe$_2$O$_4$/gCN	KOH 0.1 M	$\approx$0 [b]	[26]
NiFe$_2$O$_4$/gCN		$\approx$0 [b]	
Ni-Fe-O/gCN [f]	HClO$_4$ (pH = 3)	$\approx$ 0.35 [b]	[18]
Co^{2+}- gCN [g]	Na$_2$SO$_4$ 0.2 M	$\approx$55 [c]	[19]
TiO$_2$-Ni-CN$_x$ [e,h]	Na$_2$SO$_4$ 0.5 M (pH = 6)	$\approx$ 70 [c]	[25]
Zn-CN$_x$ [e,h]	Na$_2$SO$_4$ 0.5 M	$\leq$ 0.22 [c,i]	[27]
Mo-CN$_x$ [e,h]	Na$_2$SO$_4$ 0.2 M	$\approx$ 1.5 [c,l]	[28]
W-CN$_x$ [e,h]		$\approx$ 1.7 [c,l]	

Table S3. OER performances of selected electrocatalysts based on carbon nitride and transition metal oxides. [a] gCN = graphitic carbon nitride; [b] dark conditions; [c] light conditions; [d] = @ 1.0 eV *vs.* RHE (values at bias > 1.3 V not available); [e] CN$_x$ = polymeric carbon nitride; [f] Ni-Fe-O = mixed nickel-iron oxides; [g] cobalt-incorporated carbon nitride films; [h] atomically dispersed Ni, Zn, Mo, W-containing sites.; [i] @ 0.4 V *vs.* RHE; [l] @ 0.8 V *vs.* RHE.

In order to evaluate the system stability, Cu_xO-functionalized samples were also subjected to XPS analysis after completion of the tests indicated in Fig. S18. In this regard, Fig. S19 compares the XPS survey spectra of two representative as-prepared systems with the homologous samples after OER characterization. As can be observed, carbon, nitrogen, oxygen and copper signals were still clearly visible after functional tests, indicating a good operational stability of the synthesized materials. In addition, for *post-operando* measurements, potassium presence was also detected due to traces of KOH, used as electrolyte during water splitting experiments.
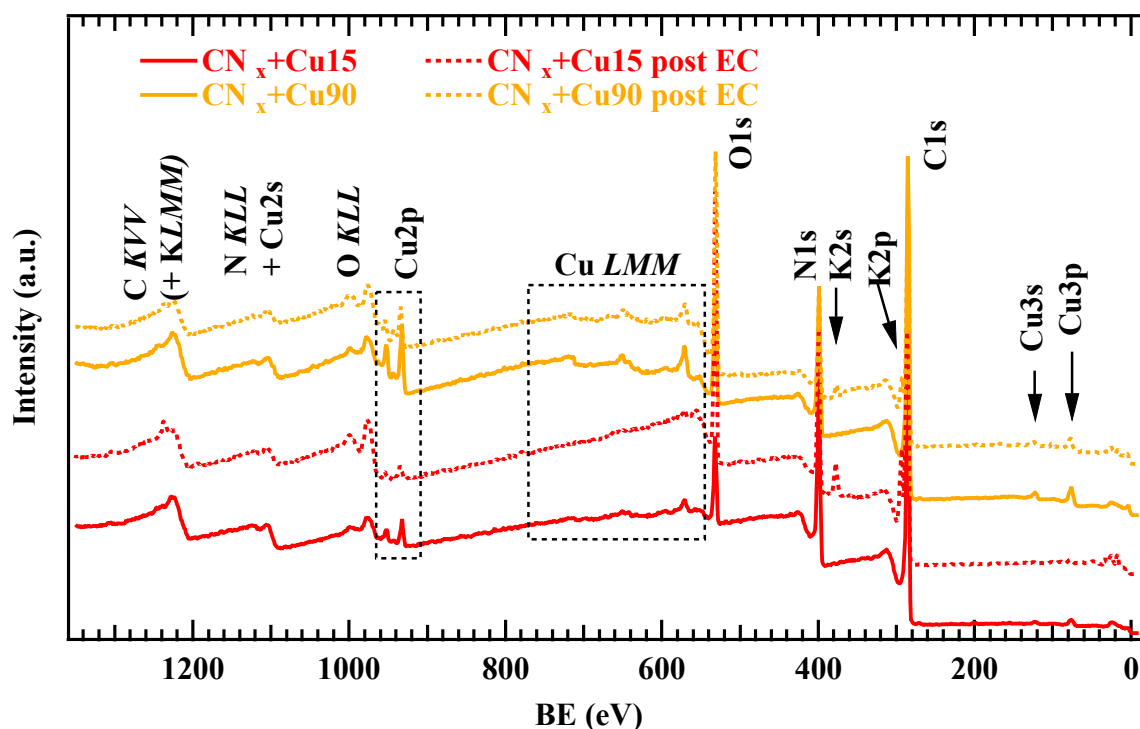

Fig. S19. XPS survey spectra for samples CN_x+Cu15 and CN_x+Cu90, as-prepared and after completion of the tests indicated in Fig. S18 (CN_x+Cu15 post EC, CN_x+Cu90 post EC).

Table S4 reports the C, N, O and Cu atomic percentages for the analysed samples, together with the corresponding N/C and Cu/N ratios. As can be observed, an increase in the oxygen atomic percentage occurs upon passing from a given as-prepared sample to the homologous one after electrochemical tests. This phenomenon is attributable to the contact of specimens with the solution used for the OER tests, which inevitably involves the adsorption of different oxide species on the electrode surface. Nevertheless, it is worthwhile observing that the N/C ratio for a given specimen does not undergo significant variations upon electrochemical testing (see Table S4). This result underscores the good stability of the synthesized carbon nitride films. Similar conclusions can also be drawn for copper particles, although the Cu/N ratio reveals, for the CN_x+Cu15 specimen, a slight

metal loss (not observed for CN_x+Cu90), likely due to the small size of copper aggregates in this sample.

Sample	CN_x+Cu15	CN_x+Cu15 post_EC	CN_x+Cu90	CN_x+Cu90 post_EC
C at.%	66.4	55.7	68.7	58.8
N at.%	25.5	21.2	19.7	17.0
O at.%	7.3	22.6	9.7	22.4
Cu at.%	0.8	0.5	1.9	1.8
N/C	0.38	0.38	0.29	0.29
Cu/N	0.032	0.024	0.10	0.11

Table S4. XPS surface atomic percentages, N/C, and Cu/N ratios for the indicated specimens. The reported values have been calculated excluding the contribution of potassium.
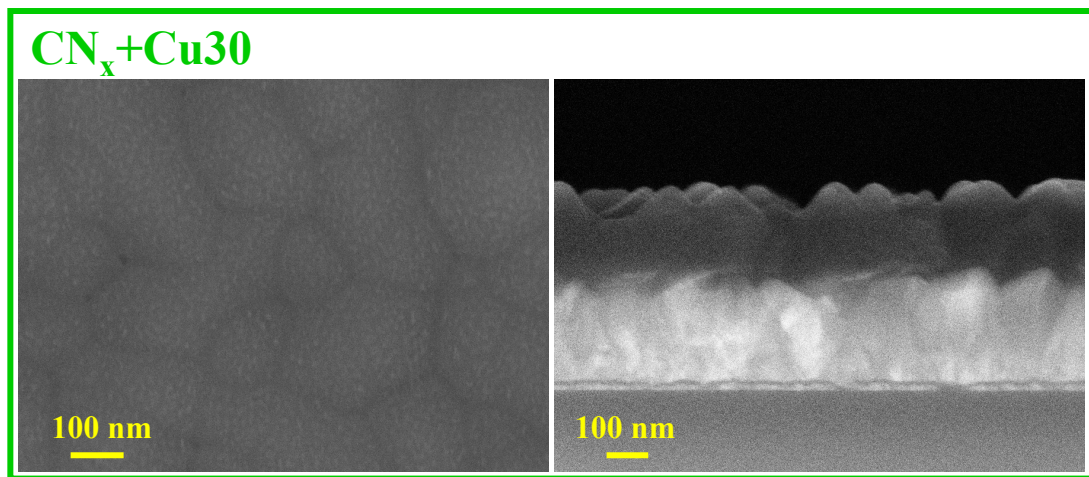
Fig. S20. Plane-view (left panel) and cross-sectional (right panel) for specimen CN$_x$+Cu30, after completion of the tests indicated in Fig. S18.

§ S3. References

1   M. Benedet, A. Gallo, C. Maccato, G. A. Rizzi, D. Barreca, O. I. Lebedev, E. Modin, R. McGlynn, D. Mariotti and A. Gasparotto, *ACS Appl. Mater. Interfaces*, 2023, **15**, 47368-47380.

2   M. Benedet, G. A. Rizzi, A. Gasparotto, O. I. Lebedev, L. Girardi, C. Maccato and D. Barreca, *Chem. Eng. J.*, 2022, **448**, 137645.

3   Y. Jiang, Z. Sun, C. Tang, Y. Zhou, L. Zeng and L. Huang, *Appl. Catal., B*, 2019, **240**, 30-38.

4   W. Liu, Z. Zhang, D. Zhang, R. Wang, Z. Zhang and S. Qiu, *RSC advances*, 2020, **10**, 28848-28855.

5   A. Korsunsky, M. McGurk, S. Bull and T. Page, *Surf. Coat. Technol.*, 1998, **99**, 171-183.

6   W. C. Oliver and G. M. Pharr, *J. Mater. Res.*, 1992, **7**, 1564-1583.

7   W. C. Oliver and G. M. Pharr, *J. Mater. Res.*, 2004, **19**, 3-20.

8   EN ISO 20502:2016 - Fine ceramics (advanced ceramics, advanced technical ceramics) - Determination of adhesion of ceramic coatings by scratch testing (ISO 20502:2005 including Cor 1:2009).

9   D. Barreca, G. Carraro, A. Gasparotto, C. Maccato, M. E. Warwick, K. Kaunisto, C. Sada, S. Turner, Y. Gönüllü and T. P. Ruoko, *Adv. Mater. Interfaces*, 2015, **2**, 1500313.

10 M. Benedet, G. A. Rizzi, O. I. Lebedev, V. Roddatis, C. Sada, J.-L. Wree, A. Devi, C. Maccato, A. Gasparotto and D. Barreca, *J. Mater. Chem. A*, 2023, **11**, 21595-21609.

11 M. Benedet, G. A. Rizzi, A. Gasparotto, N. Gauquelin, A. Orekhov, J. Verbeeck, C. Maccato and D. Barreca, *Appl. Surf. Sci.*, 2023, **618**, 156652.

12 A. Fitzgerald, L. Jiang, M. Rose and T. Dines, *Appl. Surf. Sci.*, 2001, **175**, 525-530.

13 N. Hellgren, M. P. Johansson, E. Broitman, L. Hultman and J.-E. Sundgren, *Phys. Rev. B*, 1999, **59**, 5162.

14 I. Bertóti, M. Mohai and K. László, *Carbon*, 2015, **84**, 185-196.

15 M. Benedet, G. A. Rizzi, A. Gasparotto, L. Zeng, G. Pagot, E. Olsson, V. Di Noto, C. Maccato and D. Barreca, *RSC Adv.*, 2024, **14**, 7221-7228.

16 M. Benedet, A. Gasparotto, G. A. Rizzi, C. Maccato, D. Mariotti, R. McGlynn and D. Barreca, *Surf. Sci. Spectra*, 2023, **30**, 024018.

17 S. Bull, *Surf. Coat. Technol.*, 1991, **50**, 25-32.

18 R. Wang, K. Pan, D. Han, J. Jiang, C. Xiang, Z. Huang, L. Zhang and X. Xiang, *ChemSusChem*, 2016, **9**, 2470-2479.

19 Z. Chen, H. Wang, J. Xu and J. Liu, *Chem. Asian J.*, 2018, **13**, 1539-1543.

20 G. Zhang, S. Zang and X. Wang, *ACS Catal.*, 2015, **5**, 941-947.

21 H. Wang, T. Sun, L. Chang, P. Nie, X. Zhang, C. Zhao and X. Xue, *Electrochim. Acta*, 2019, **303**, 110-117.

22 S. Ohn, S. Y. Kim, S. K. Mun, J. Oh, Y. J. Sa, S. Park, S. H. Joo, S. J. Kwon and S. Park, *Carbon*, 2017, **124**, 180-187.

23 J. Yan, H. Wu, H. Chen, L. Pang, Y. Zhang, R. Jiang, L. Li and S. Liu, *Appl. Catal., B*, 2016, **194**, 74-83.

24 S. Kumar, N. L. Reddy, A. Kumar, M. V. Shankar and V. Krishnan, *Int. J. Hydrogen Energy*, 2018, **43**, 3988-4002.

25 S. F. Blaskievicz, H. L. S. Santos, I. F. Teixeira, J. L. Bott-Neto, P. S. Fernández and L. H. Mascaro, *Mater. Today Nano*, 2022, **18**, 100192.

26 J. Chen, D. Zhao, Z. Diao, M. Wang and S. Shen, *Sci. Bull.*, 2016, **61**, 292-301.

27 D. Zhao, Y. Wang, C.-L. Dong, F. Meng, Y.-C. Huang, Q. Zhang, L. Gu, L. Liu and S. Shen, *Nano-Micro Lett.*, 2022, **14**, 223.

28 F. Yu, Q. Deng, H. Li, Y. Xia and W. Hou, *Appl. Catal., B*, 2023, **323**, 122180.